Research Square

Preprints are preliminary reports that have not undergone peer review.
They should not be considered conclusive, used to inform clinical practice,
or referenced by the media as validated information.

Identification of an SFRP1 inhibitor as a novel therapeutic strategy for cancers using dry-wet combined drug discovery strategy

Zhang Yunlong

t.jzhangyunlong@126.com

Tianjin Medical University Cancer Institute and Hospital

Wei Ruiqi

Tianjin Medical University

Pan Meihong

Tianjin Medical University

Qin Nan

Tianjin Medical University

Wei Xiaopeng

Tianjin Medical University

Shen Jun

Tianjin Medical University Cancer Institute and Hospital

Research Article

Keywords: Wnt signaling, SFRP1, Cancer, Molecular docking, Molecular dynamics

Posted Date: April 25th, 2026

DOI: https://doi.org/10.21203/rs.3.rs-9393160/v1

License: This work is licensed under a Creative Commons Attribution 4.0 International License.
Read Full License

Additional Declarations: No competing interests reported.

Version of Record: A version of this preprint was published at Molecular Diversity on May 27th, 2026.
See the published version at https://doi.org/10.1007/s11030-026-11586-3.

Abstract

Secreted frizzled-related protein 1 (SFRP1) exerts a context-dependent dual role in cancer, and its epigenetic silencing drives pro-tumorigenic non-canonical Wnt activation, a promising therapeutic target for advanced malignancies. In this study, a validated 3D SFRP1 model was built by comprehensive computational approach. High-throughput virtual screening of a commercial compound library identified a common core scaffold, which was rationally design to synthesize lead compound. The target molecule was synthesized via organic synthetic approaches. Surface plasmon resonance (SPR) assays confirmed the specific binding of compound **L1** to SFRP1 with a dissociation constant (KD) of 79.1 nM. Furthermore, molecular docking and molecular dynamics (MD) simulation elucidated the interaction between compound **L1** and SFRP1 at the molecular level and in physiological conditions.

Introduction

Secreted frizzled-related protein 1, a member of the secreted glycoprotein family, functions as a natural antagonist of the Wnt pathway by virtue of its cysteine-rich domain (CRD) and netrin-related domain (NTR) [1]. Traditionally regarded as a tumor suppressor, SFRP1 inhibits canonical Wnt signaling in normal tissues and early-stage tumors by competing with Frizzled receptors for Wnt ligands or directly sequestering Wnt proteins [2]. However, accumulating evidence has uncovered a context-dependent "dual role" of SFRP1 in cancer, with its functional switch tightly linked to epigenetic silencing and pathway selectivity [3]. SFRP1 exerts dual tumor-suppressive and oncogenic roles in cancer, with a tumor-type-specific mode of action.

Tumor-suppressive role: In the majority of human cancers, SFRP1 expression is downregulated via epigenetic silencing, which leads to aberrant activation of the Wnt signaling pathway. This dysregulation promotes tumorigenesis, malignant progression and metastasis, and is associated with an unfavorable clinical prognosis of cancer patients. Restoration of SFRP1 expression exerts anti-tumor effects by inhibiting the hyperactivated Wnt signaling pathway, which in turn induces cancer cell apoptosis, suppresses cell proliferation and invasion. Additionally, re-expression of SFRP1 can enhance the sensitivity of cancer cells to chemotherapeutic agents such as cisplatin and paclitaxel [4].

Oncogenic role: In specific cancer types including metastatic renal cell carcinomas [5], triple-negative breast cancer [6], gastric cancer [7], SFRP1 is abnormally upregulated. Ectopic SFRP1 expression can activate the TGF-β signaling pathway to facilitate epithelial-mesenchymal transition (EMT) and enhance the invasive potential of cancer cells. Moreover, elevated SFRP1 expression is correlated with chemoresistance and poor prognosis in patients with the aforementioned cancers. This functional switch thus highlights the therapeutic potential of targeting residual SFRP1 and its mediated non-canonical Wnt pathway in advanced tumors [8-9]. As selective SFRP1 inhibition can block the pro-tumorigenic effects of non-canonical Wnt signaling without perturbing the homeostasis of normal tissues [10].

Virtual screening, the in silico counterpart of high-throughput screening applied to large compound libraries, constitutes an integral component of the drug discovery pipeline and affords substantial reductions in the time and cost associated with novel drug development [11-12]. Structure-based high-throughput virtual screening relies on protein-ligand co-crystal structures [13]. As the 3D crystal structure of SFRP1 is not available in the RCSB Protein Data Bank (PDB), we retrieved the predicted SFRP1 structure from the AlphaFold Protein Structure Database. A comprehensive computational approach has enabled the druggability of the SFRP1 protein structure.

Methods and materials

The generation of SFRP1 protein

The 3D model of the SFRP1 protein (AF-Q8N474-F1-v6) was downloaded by visiting the AlphaFold Protein Structure Database (https://alphafold.com/) [14]. The initial procedure involved performing a 200 ns molecular dynamics simulation on the predictive protein structure to analyze the conformational changes and stability check for the modeled SFRP1.

Model validation of SFRP1 protein

In the present study, the structural quality and stereochemical validity of the predictive SFRP1 were systematically evaluated using the SAVES v6.0 server. As an integrated meta-server, SAVES v6.0 incorporates the PROCHECK and ERRAT algorithms to enable comprehensive dynamic validation of multiple stereochemical parameters for the predictive model. During structure validation, PROCHECK was utilized to generate Ramachandran plots by analyzing the phi (ϕ) and psi (ψ) dihedral angle distributions of individual amino acid residues [15]. The ERRAT module was applied to assess the non-covalent atomic interactions and overall statistical quality of the modeled protein structure [16]. Furthermore, the ProSA server was used to analyze the folding energy of the SFRP1 model relative to a large dataset of experimentally determined native protein structures [17].

Ligand Binding Site Prediction

The prediction of the active sites of the SFRP1 structure was performed using the online tool PrankWeb based on the P2Rank machine learning algorithm, which samples points on the solvent-accessible surface of the protein, calculates the ligandability of each point, and generates scores via a random forest model [18]. High-scoring points are clustered into binding pockets and ranked by their predicted scores. A major advantage of this approach is template-free nature, enabling the identification of both novel and allosteric sites with high efficiency and accuracy. Thus, PrankWeb allows rapid and reliable identification of potential ligand-binding pockets from protein structures [19].

High-throughput virtual screening based on predictive SFRP1

The LibDock module of the Discovery Studio 4.0 suite was conducted using high-throughput virtual screening [20]. The top-ranked prediction pocket was defined as binding site by selecting the key residues Ser96, Trp97, Pro99, Leu100, Asn102, Lys103, Met144, Phe147, Phe149, Tyr150, Pro152, Met154, Ala197, Glu200, His201, Ala204, Ser205, and Arg273. The “In Site Sphere parameter” was 5.755114, -4.555607, 6.421221; Raduis 13.341011 “Conformation Method” was set to “FAST”, “Max Hits to Save” was set to 1. All other parameters were set to default. The outputted compounds were sorted according to LibDock scores, with higher scores being subjected to further analysis.

The commercially available compound library (https://lifechemicals.com/) is distinguished by its extensive scale and exceptional structural diversity, rendering it a premier resource for virtual screening campaigns aimed at identifying bioactive molecules and lead-like scaffolds [21]. For the present study, a curated library of 3.4 million compounds were subjected to virtual screening for hit compounds discovery, following rigorous preprocessing via the Prepare Ligands protocol. This systematic pre-treatment workflow entailed the elimination of duplicate structures, generation of three-dimensional molecular conformations, and exclusion of compounds possessing unfavorable physicochemical properties that would preclude their utility as viable drug candidates.

Molecular dynamics (MD) simulation

The optimal complex obtained from molecular docking screening was subjected to 200 ns MD simulations using the GROMACSv2023.3 [22]. Prior to simulation, hydrogen atoms were added to the ligand, and the protein structure was optimized using Avogadro. The simulation system was constructed with the Amber94 force field for the protein and the Generalized Amber Force Field (GAFF) for the ligand [23], respectively. The complex was solvated in a orthorhombic box filled with the TIP3P water model, and Na^+/Cl^- ions were added to neutralize the system charge. The simulation protocol consisted of a 200 ps equilibration in the canonical ensemble (NVT) followed by a 200 ps equilibration in the isothermal-isobaric ensemble (NPT). Subsequently, 200 ns production MD simulations were performed with a time step of 2 fs. The binding stability of the complex was systematically evaluated by analyzing multiple parameters including root-mean-square deviation (RMSD), root-mean-square fluctuation (RMSF), radius of gyration (Rg), solvent-accessible surface area (SASA), hydrogen bond interactions as well as Gibbs energy landscape [24].

Design and synthesis of target compound

The structurally skeletons and their analogs that frequently appeared in the high-throughput virtual screening results, cluster analysis was performed to evaluate the rationality of their binding conformations and synthetic feasibility. The common skeletons were retained to the greatest extent, while atoms or groups that made no contribution to the binding affinity with the receptor were removed. In this study, the synthesis of target products was achieved by employing classic organic synthetic reactions, which featured readily available starting materials and high yields. Specifically, the construction of the biphenyl structural core was accomplished via the classic Suzuki-Miyaura coupling

reaction [25]; the establishment of the amide chain linker was realized through the amide condensation reaction. Finally, nuclear magnetic resonance (NMR) spectroscopy and high-resolution mass spectrometry (HRMS) were comprehensively used to characterize the structures of the intermediate and target product.

Surface plasmon resonance (SPR) assays

The recombinant human SFRP1 protein (Active) (ab288782) was purchased from Abcam (https://www.abcam.cn/).

Compound **L1** was dissolved in dimethyl sulfoxide (DMSO) to yield a series of stock solutions at different concentrations. Phosphate-buffered saline containing Tween 20 was employed as the running buffer throughout the assay. Briefly, the buffer was delivered at the maximum flow rate until a stable baseline was achieved, followed by complete removal of air bubbles. The sensor chip surface was regenerated with 10 mM HCl and equilibrated for 1 min. The flow rate of PBST was then adjusted to 10 μL/min, and the carboxyl-functionalized (COOH) sensor chip was activated by injecting 100 μL of a 1:1 mixture of 1-ethyl-3-(3-dimethylaminopropyl)carbodiimide and N-hydroxysuccinimide (EDC/NHS), with a 4-min contact time. Both compound **L1** and SFRP1 protein were diluted using the activation buffer. Prior to sample injection, the injection port was rinsed with running buffer to eliminate residual air. Subsequently, 200 μL of blocking solution was injected at 20 μL/min for 4 min, and the sample loop was flushed with buffer to remove air bubbles. The system was equilibrated for 5 min to establish a stable baseline. Serial dilutions of the candidate compound were prepared and injected onto the chip in ascending order of concentration. Kinetic parameters characterizing the binding interactions were determined and analyzed using Biacore Insight Evaluation Software [26].

ResultS

Prediction of the three-dimensional structure and active pocket of SFRP1

During the initial phase of the MD simulation, the protein backbone exhibited significant fluctuations, which was primarily attributed to conformational relaxation. Subsequently, the RMSD plateaued at approximately 1.9 nm, indicating structural stabilization (**Fig**.**1a**). Structural alignment of the initial and conformations cluster yielded a RMSD value of 4.532 Å (**Fig**. **1b**) demonstrates the instability of the initial conformation. The potential active pocket of SFRP1 was predicted by employing a physics-based scoring function combined with a Random Forest machine learning model to enhance the accuracy of pocket predictions. The plot displays the top three predicted results with AlphaFold confidence mode (**Fig**.**1c**). The predicted active sites and detailed parameters were presented in **Table 1**. Among the three predicted binding pockets, the top ranked site yielded a prediction score of 10.43, which was considerably higher than those of the other two. This pocket, composed of 19 amino acid residues, exhibited a distinct geometric conformation and high sequence conservation, making it rational for subsequent virtual screening (**Fig**.**1d**). As illustrated in **Fig. 1(e)** and **1(f)**, the electrostatic potential and

hydrophobicity of SFRP1 were analyzed. The predicted active site was found to exhibit moderate electrostatic potential and comparatively high hydrophobicity.

Table1 The parameters of predicting pocket

Rank	Score	Probability	Num.of residues	Pocket center	Residues
1	10.43	0.537	19	-5.6103, 3.8707, -1.8507	Ser96, Trp97, Pro99, Leu100, Asn102, Lys103, Met144, Phe147, Phe149, Tyr150, Pro152, Met154, Ala197, Glu200, His201, Ala204, Ser205, Arg273, and Lys286
2	2.58	0.060	8	13.2289, 1.9663, -14.0423	Gln110, Val111, Cys114, Ser115, Val120, Ile167, Val71, Tyr73.
3	1.55	0.020	7	-4.1801, -6.62755, -18.1028	Glu134, Arg137, Glu141, Trp151, Lys156, Cys157, Asp158.

Structural validation of the predicted SFRP1 model was systematically executed through a multi-dimensional approach employing PROCHECK, ERRAT, PROSA servers. The PROCHECK analysis demonstrated excellent stereo chemical quality: 83.8% of residues lay in the most favored regions, 14.4% in the allowed regions, and 1.1% in the generously allowed regions, with merely 0.7% in the disallowed regions. This distribution confirmed the absence of aberrant dihedral bond angles or distorted 3D backbone conformations. Assessment by the ERRAT algorithm, which evaluates non-bonded atom interactions, yielded a score of 87.234. This value surpasses the threshold of 50 for high-quality models, substantiating the reliability of the constructed SFRP1 structure. Concurrent validation via the PROSA web server, based on the Z-score, indicated that the SFRP1 model possessed a native-like energy profile with a Z-score of -6.75, further affirming its structural superiority over the template. Collectively, these results corroborate the reliability of the SFRP1 model, and all detailed outputs are presented in the Supplementary information.

Following structure-based virtual screening for a commercial compound library, a class of structurally analogous compounds was identified, as illustrated below (**Fig. 2a**). These compounds were docked into the predicted ligand-binding pocket and are characterized by a biphenyl core, a substituted five or six-membered heterocyclic moiety, an amide linkage, and generally contain one chiral center. However, compound library retrieval revealed that all such compounds existed as racemates with only 90% purity, which did not meet the requirements for subsequent biological activity evaluation. Therefore, based on the screening results, we hypothesized that this class of scaffolds could genuinely bind to SFRP1. To verify this hypothesis, we performed rational compound design on this scaffold. First, the biphenyl core was retained, and a fluorophenyl moiety, a privileged fragment in many bioactive agents, was introduced. To reduce synthetic difficulty, the chiral center was eliminated, and the linker was modified to a two-

carbon amide chain. Meanwhile, a pyrimidine ring ring with two hydrogen-bond acceptors was selected as the heterocyclic moiety. The detailed design strategy is described as follows (**Fig. 2b**).

Synthesis of the target product

The detail synthesis scheme was shown as **Fig.3**. 4-Bromophenethylamine (10 mmol, 1.0 eq) and pyrimidine-5-carboxylic acid (10 mmol, 1.0 eq) were added to a reaction flask and dissolved in dichloromethane. HOBT (11 mmol, 1.1 eq) and EDCI (11 mmol, 1.1 eq) were added successively, and the mixture was stirred at room temperature for 24 h to complete the reaction. The reaction mixture was diluted with CH_2Cl_2, and the organic phase was washed with water three times, dried over anhydrous sodium sulfate, and collected. The organic layer was concentrated under reduced pressure to afford the crude intermediate S1, which was used in the next reaction without further purification.

S1 (0.33 mmol, 1.0 eq) was accurately weighed and placed in a reaction flask, followed by the addition of 550 μL of 1,4-dioxane for dissolution; the substrate showed poor solubility. An additional 110 μL of deionized water was then added, and the mixture was sonicated to achieve complete dissolution of the starting material. Cesium carbonate (1.64 mmol, 5.0 eq) was weighed and added to the reaction flask, followed by 3-fluorophenylboronic acid (0.66 mmol, 2 eq). Subsequently, 2-dicyclohexylphosphino-2',4',6'-triisopropylbiphenyl (0.16 mmol, 0.5 eq) and [1,1'-bis(diphenylphosphino)ferrocene]dichloropalladium(II) (0.26 mmol, 0.8 eq) were successively added to the flask. The reaction system was subjected to repeated vacuum-nitrogen exchange for deaeration, then stirred and heated at 100 °C for 18 h under a nitrogen atmosphere in an oil bath. The reaction progress was monitored by thin-layer chromatography (TLC, CH_2Cl_2/CH_3OH = 50:1, v/v), and the reaction was terminated upon complete consumption of the starting material. The reaction mixture was concentrated under reduced pressure at 65 °C to remove 1,4-dioxane and water. The resulting residue was filtered through a pad of celite on filter paper to remove palladium species, and the celite pad was rinsed with ethyl acetate. The combined filtrate was extracted with ethyl acetate, and the organic phase was washed successively with saturated aqueous sodium bicarbonate (3 times), deionized water (2 times) and saturated brine (2 times). The organic layer was dried over anhydrous $MgSO_4$, filtered and concentrated under reduced pressure to afford a brown crude product. Purification of the crude product was performed by flash column chromatography on silica gel (eluent: petroleum ether/ethyl acetate = 1.5:1 to 1:1.5, v/v) to give the pure product as a white solid.

The chemical structure of the target compound was confirmed by NMR, HRMS spectroscopy.

N-(4-bromophenethyl)pyrimidine-5-carboxamide (**S1**)

White powder, yield: 91.22%. ^{1}H NMR (400 MHz, $CDCl_3$): *δ* 9.23 (s, 1H), 8.99 (s, 2H), 7.39 (d, *J* = 8.0 Hz, 2H), 7.38 (d, *J* = 8.0 Hz, 2H), 7.06 (d, *J* = 8.0 Hz, 2H), 6.63 (s, 1H), 3.67 (q, *J* = 16.0, 8.0 Hz, 2H), 2.87 (t, *J* = 8.0 Hz, 2H).^{13}C NMR (100 MHz, $CDCl_3$): *δ* 163.56, 160.48, 155.49, 137.35, 131.89, 130.45, 127.86, 120.70, 35.85, 34.92.

N-(2-(3'-fluoro-[1,1'-biphenyl]-4-yl)ethyl)pyrimidine-5-carboxamide(L1)

White powder, yield: 55.76%. ^{1}H-NMR (400 MHz, DMSO-d_6) :δ 9.31 (1H, s), 9.13 (2H, s), 8.96 (1H, t, J = 5.2Hz), 7.66 (2H, d, J = 8.0 Hz), 7.50-7.45 (3H, m), 7.36 (2H, d, J = 8.0 Hz), 7.19-7.15 (1H, m), 3.56 (2H, q, J = 6.7 Hz), 2.91 (2H, t, J = 7.2 Hz).^{13}C-NMR(100 MHz, DMSO-d_6): δ 163.5 (C), 163.3 (C, $^{1}J_{C\text{-}F}$ = 241.6 Hz), 160.4 (C), 156.2 (C), 142.9 (C, $^{3}J_{C\text{-}F}$ = 7.8 Hz), 139.8 (C), 137.2 (C), 131.3 (CH, $^{3}J_{C\text{-}F}$ = 8.5 Hz), 129.8 (CH), 128.4 (C), 127.3 (CH), 123.0 (CH, $^{4}J_{C\text{-}F}$ = 2.51Hz), 114.4 (CH, $^{2}J_{C\text{-}F}$ = 20.9 Hz),113.6 (CH, $^{2}J_{C\text{-}F}$ = 21.8 Hz), 41.2 (CH_2), 34.9 (CH_2). ^{19}F-NMR (376 MHz, DMSO-d_6): δ -112.86 (1F, s).

ESI-HRMS: m/z, calc. for $C_{19}H_{17}FN_3O$ ($[M+H]^+$): 322.1356; found: 322.1348

SPR analysis of the binding affinity between SFRP1 and L1

The real-time SPR sensorgrams display the concentration-dependent binding and dissociation profiles of compound L1 interacting with its immobilized target (Fig.4a). Analytes at gradient concentrations (625, 313, 156, 78, 39, and 19 nM) were injected over the sensor surface, resulting in distinct association and dissociation phases. In the association phase (0–100 s), the response values (RU) increased rapidly in a concentration-dependent manner, with the highest RU observed at 625 nM and the lowest at 19 nM. Following analyte injection, a gradual dissociation phase was observed, and no complete return to baseline was detected, indicating a stable binding complex formed between L1 and SFRP1. The equilibrium binding response (RU) at the end of the association phase was plotted against the analyte concentration (nM) and fitted using a standard affinity model (Fig.4b). The derived equilibrium dissociation constant (KD) was calculated to be 79.1 nM. Collectively, these data demonstrate that L1 exhibits specific and concentration-dependent binding to SFRP1 with a stonger binding affinity within the range typically observed for bioactive molecules.

Molecular docking analysis the interactions between L1 and the target.

Compound **L1** bound to the predicted binding pocket of SFRP1 protein, and its docking conformation was shown in **Fig**.**5a**. It can be clearly observed that **L1** was embedded in the predicted active site in a relatively extended conformation, forming interactions with the surrounding amino acid residues of the pocket, including Ser96, Trp97, Phe147, Tyr150, Pro152, Glu153 and Lys314 (**Fig.5b**). Specifically, the fluorobenzene forms a Pi-Alkyl interaction with Phe147; the aromatic benzene ring generates a Pi-Cation interaction with Tyr150; the oxygen atom on the linker chain forms one hydrogen bond with Ser96. Moreover, the nitrogen atom on the pyrimidine ring forms one strong hydrogen bond with Glu153, one Pi-Alkyl interaction with Pro152, one Pi-Anion interaction with Lys314, respectively (**Fig.5c**).

MD simulation

The 200 ns MD simulation was performed to further validate the interaction of the SFRP1-**L1** complex. Firstly, the RMSD value of the SFRP1-**L1** complex described in **Fig.6a** was observed to exhibit a transient phase between 0 and 50 ns. However, it remained between 0.5 nm and 0.9 nm and tended to steady state. In addition, in order to identify the lowest energy conformation of SFRP1-**L1** complex. The RMSF

plot of SFRP1-L1 complex was illustrated in **Fig**. **6b**, residues 0–60 exhibited relatively large fluctuations exceeding 1 nm, whereas residues in other regions showed much smaller fluctuations. All amino acid residues in the active site displayed fluctuations below 0.3 nm, indicating that the ligand-binding pocket is structurally conserved and that the ligand can stably bind to the predicted binding site. Several H-bonds were observed between the SFRP1-**L1** complex during simulation (**Fig**. **6c**). For the SFRP1-**L1** complex, the total Rg values were around 2.5 nm (**Fig**. **6d**). The average SASA for complexes was 180 nm^2 (**Fig**. **6e**). All these parameters remained stable throughout the MD simulation, confirming the structural stability of the SFRP1-**L1** complex.

The 2D FEL projected onto the root-mean-square deviation (RMSD, X-axis) and radius of gyration (Rg, Y-axis) reveals a continuous low-free-energy pathway traversing from the upper-left region (RMSD≈0.21, Rg≈2.43) toward the lower-right region (RMSD≈0.65, Rg≈2.25). The global free energy minimum, depicted by the deep-blue basin, is localized at high RMSD and low Rg, corresponding to the thermodynamically most stable conformational state of the system **(Fig.7a)**. The corresponding 3D surface plot illustrates the rugged nature of the free energy surface, with free energy defined as the Z-axis. A prominent deep valley corresponds to the global free energy minimum, flanked by high-energy barriers (red peaks) that define the boundaries of accessible conformational space. This 3D FEL plot confirms the continuous conformational transition observed in the 2D heatmap, and shows that the SFRP1-**L1** complex tends to adopt a more compact conformation with lower Rg and higher RMSD (**Fig.7b**).

Discussion

In a virtual screening study targeting SFRP1 inhibitors, Muralidharan Jothimani *et al* [8] constructed a homology model of SFRP1 and analyzed its specific active sites. Computational study was then performed against a pocket defined by Arg5, Arg11, Ala13, Lys245, Lys274, Phe147, Pro99, and Ser277. In the present study, virtual screening was carried out based on the ligand-binding site defined by Ser96, Trp97, Pro99, Leu100, Asn102, Lys103, Met144, Phe147, Phe149, Tyr150, Pro152, Met154, Ala197, Glu200, His201, Ala204, Ser205, Arg273, and Lys286. Regarding the selection of ligand-binding residues, several positions in this study (e.g., Pro99 and Phe147) are consistent with those reported in previous work. Experimental results from *in vitro* binding assays suggest that the SFRP1 ligand-binding site adopted in the present study may be more accurate.

Among the multifaceted signaling networks implicated in carcinogenesis, the Wnt pathway stands out as a paradigmatic regulator, encompassing two functionally distinct branches: the canonical Wnt/β-catenin pathway and non-canonical Wnt pathways [27]. Despite these advancements, the translation of SFRP1 inhibitors into clinical practice remains hindered by the lack of systematic evaluation of their efficacy across SFRP1-silenced tumor types and incomplete understanding of their mechanism of action in targeting non-canonical Wnt signaling [28-29] In this study, we designed and synthesized a potent SFRP1 inhibitor, **L1**, which can block the pro-tumorigenic non-canonical Wnt signaling and thus exert anti-tumor effects in SFRP1-epigenetically silenced malignancies [30]. This study will not only provide

novel therapeutic agents for precision oncology but also deepen our understanding of the context-dependent functions of SFRP1 in cancer, paving the way for the development of pathway-targeted strategies for unmet clinical needs.

Conclusion

This study adopted an integrated combined drug discovery strategy to develop a novel selective SFRP1 inhibitor for cancers characterized by SFRP1 epigenetic silencing and non-canonical Wnt pathway activation. A reliable predictive 3D model of SFRP1 was constructed via AlphaFold, refined by 200 ns MD simulations, and validated by PROCHECK, ERRAT, and ProSA. A top-ranked conserved ligand-binding pocket was identified for high-throughput virtual screening of a compound library. A hit core scaffold was identified and rationally optimized to afford the target compound **L1**, whose structure was confirmed by NMR and HRMS. The binding affinity between **L1** and SFRP1 was characterized by SPR assays, revealing concentration-dependent and stable binding. Molecular docking revealed that **L1** formed multiple specific intermolecular interactions with key pocket residues to stabilize the binding conformation, and 200 ns MD simulations of SFRP1-**L1** complex confirmed its structural stability. This study establishes a validated 3D model of SFRP1 and an optimized dry-wet drug discovery pipeline for developing SFRP1 inhibitors. We also identify a novel SFRP1 inhibitor **L1**, which provides an experimental and theoretical basis for precision oncology targeting SFRP1-mediated non-canonical Wnt signaling.

Declarations

Funding

The authors have no relevant financial or non-financial interests to disclose.

Conflict of Interest Statement:

The authors declare no known competing economic interests or personal relationships that could have influenced this work reported herein.

References

1. Bhat, R. A., Stauffer, B., Komm, B. S., and Bodine, P. V. (2007) Structure-function analysis of secreted frizzled-related protein-1 for its Wnt antagonist function, J Cell Biochem 102, 1519-1528.
2. Surana, R., Sikka, S., Cai, W., Shin, E. M., Warrier, S. R., Tan, H. J., Arfuso, F., Fox, S. A., Dharmarajan, A. M., and Kumar, A. P. (2014) Secreted frizzled related proteins: Implications in cancers, Biochim

Biophys Acta 1845, 53-65.

3. Baharudin, R., Tieng, F. Y. F., Lee, L. H., and Ab Mutalib, N. S. (2020) Epigenetics of SFRP1: The Dual Roles in Human Cancers, Cancers (Basel) 12.
4. Zhang, W., Zhang, K., Ma, Y., Song, Y., Qi, T., Xiong, G., Zhang, Y., Kan, C., Zhang, J., Han, F., and Sun, X. (2023) Secreted frizzled-related proteins: A promising therapeutic target for cancer therapy through Wnt signaling inhibition, Biomed Pharmacother 166, 115344.
5. Saini, S., Liu, J., Yamamura, S., Majid, S., Kawakami, K., Hirata, H., and Dahiya, R. (2009) Functional significance of secreted Frizzled-related protein 1 in metastatic renal cell carcinomas, Cancer Res 69, 6815-6822.
6. Bernemann, C., Hulsewig, C., Ruckert, C., Schafer, S., Blumel, L., Hempel, G., Gotte, M., Greve, B., Barth, P. J., Kiesel, L., and Liedtke, C. (2014) Influence of secreted frizzled receptor protein 1 (SFRP1) on neoadjuvant chemotherapy in triple negative breast cancer does not rely on WNT signaling, Mol Cancer 13, 174.
7. Qu, Y., Ray, P. S., Li, J., Cai, Q., Bagaria, S. P., Moran, C., Sim, M. S., Zhang, J., Turner, R. R., Zhu, Z., Cui, X., and Liu, B. (2013) High levels of secreted frizzled-related protein 1 correlate with poor prognosis and promote tumourigenesis in gastric cancer, Eur J Cancer 49, 3718-3728.
8. Jothimani, M., Vijayaraghavalu, S., Sadasivam, K., and Muthusamy, K. (2025) Identification of Potent SFRP1 Inhibitors for Colorectal Cancer using a Comprehensive Computational Approach, Curr Comput Aided Drug Des 21, 1022-1035.
9. Caldwell, G. M., Jones, C., Gensberg, K., Jan, S., Hardy, R. G., Byrd, P., Chughtai, S., Wallis, Y., Matthews, G. M., and Morton, D. G. (2004) The Wnt antagonist sFRP1 in colorectal tumorigenesis, Cancer Res 64, 883-888.
10. Zhao, H., Ming, T., Tang, S., Ren, S., Yang, H., Liu, M., Tao, Q., and Xu, H. (2022) Wnt signaling in colorectal cancer: pathogenic role and therapeutic target, Mol Cancer 21, 144.
11. Subramaniam, S., Mehrotra, M., and Gupta, D. (2008) Virtual high throughput screening (vHTS)--a perspective, Bioinformation 3, 14-17.
12. Banegas-Luna, A. J., Ceron-Carrasco, J. P., and Perez-Sanchez, H. (2018) A review of ligand-based virtual screening web tools and screening algorithms in large molecular databases in the age of big data, Future Med Chem 10, 2641-2658.
13. Wang, S., Jiang, J. H., Li, R. Y., and Deng, P. (2020) Docking-based virtual screening of TbetaR1 inhibitors: evaluation of pose prediction and scoring functions, BMC Chem 14, 52.
14. Varadi, M., Bertoni, D., Magana, P., Paramval, U., Pidruchna, I., Radhakrishnan, M., Tsenkov, M., Nair, S., Mirdita, M., Yeo, J., Kovalevskiy, O., Tunyasuvunakool, K., Laydon, A., Zidek, A., Tomlinson, H., Hariharan, D., Abrahamson, J., Green, T., Jumper, J., Birney, E., Steinegger, M., Hassabis, D., and Velankar, S. (2024) AlphaFold Protein Structure Database in 2024: providing structure coverage for over 214 million protein sequences, Nucleic Acids Res 52, D368-D375.
15. Laskowski, R. A., Rullmannn, J. A., MacArthur, M. W., Kaptein, R., and Thornton, J. M. (1996) AQUA and PROCHECK-NMR: programs for checking the quality of protein structures solved by NMR, J

Biomol NMR 8, 477-486.

16. Colovos, C., and Yeates, T. O. (1993) Verification of protein structures: patterns of nonbonded atomic interactions, Protein Sci 2, 1511-1519.
17. Wiederstein, M., and Sippl, M. J. (2007) ProSA-web: interactive web service for the recognition of errors in three-dimensional structures of proteins, Nucleic Acids Res 35, W407-410.
18. Krivak, R., and Hoksza, D. (2018) P2Rank: machine learning based tool for rapid and accurate prediction of ligand binding sites from protein structure, J Cheminform 10, 39.
19. Polak, L., Skoda, P., Riedlova, K., Krivak, R., Novotny, M., and Hoksza, D. (2025) PrankWeb 4: a modular web server for protein-ligand binding site prediction and downstream analysis, Nucleic Acids Res 53, W466-W471.
20. Rao, S. N., Head, M. S., Kulkarni, A., and LaLonde, J. M. (2007) Validation studies of the site-directed docking program LibDock, J Chem Inf Model 47, 2159-2171.
21. Alrouji, M., Yasmin, S., Alshammari, M. S., Alhumaydhi, F. A., Sharaf, S. E., Shahwan, M., and Shamsi, A. (2025) Virtual screening and molecular dynamics simulations identify repurposed drugs as potent inhibitors of Histone deacetylase 1: Implication in cancer therapeutics, PLoS One 20, e0316343.
22. Abraham, M. J., Murtola, T., Schulz, R., Páll, S., Smith, J. C., Hess, B., and Lindahl, E. (2015) GROMACS: High performance molecular simulations through multi-level parallelism from laptops to supercomputers, SoftwareX 1-2, 19-25.
23. Wang, J., Wolf, R. M., Caldwell, J. W., Kollman, P. A., and Case, D. A. (2004) Development and testing of a general amber force field, J Comput Chem 25, 1157-1174.
24. Li, L., Mohammed, A. H., Auda, N. A., Alsallameh, S. M. S., Albekairi, N. A., Muhseen, Z. T., and Butch, C. J. (2024) Network Pharmacology, Molecular Docking, and Molecular Dynamics Simulation Analysis Reveal Insights into the Molecular Mechanism of Cordia myxa in the Treatment of Liver Cancer, Biology (Basel) 13.
25. Tatamidani, H., Kakiuchi, F., and Chatani, N. (2004) A new ketone synthesis by palladium-catalyzed cross-coupling reactions of esters with organoboron compounds, Org Lett 6, 3597-3599.
26. Pattnaik, P. (2005) Surface plasmon resonance: applications in understanding receptor-ligand interaction, Appl Biochem Biotechnol 126, 79-92.
27. Zhan, T., Rindtorff, N., and Boutros, M. (2017) Wnt signaling in cancer, Oncogene 36, 1461-1473.
28. Vincent, K. M., and Postovit, L. M. (2017) A pan-cancer analysis of secreted Frizzled-related proteins: re-examining their proposed tumour suppressive function, Sci Rep 7, 42719.
29. Kahn, M. (2014) Can we safely target the WNT pathway?, Nat Rev Drug Discov 13, 513-532.
30. Losada-Garcia, A., Salido-Guadarrama, I., Cortes-Ramirez, S. A., Cruz-Burgos, M., Morales-Pacheco, M., Vazquez-Santillan, K., Rodriguez-Martinez, G., Gonzalez-Ramirez, I., Gonzalez-Covarrubias, V., Perez-Plascencia, C., and Rodriguez-Dorantes, M. (2023) SFRP1 induces a stem cell phenotype in prostate cancer cells, Front Cell Dev Biol 11, 1096923.

Figures

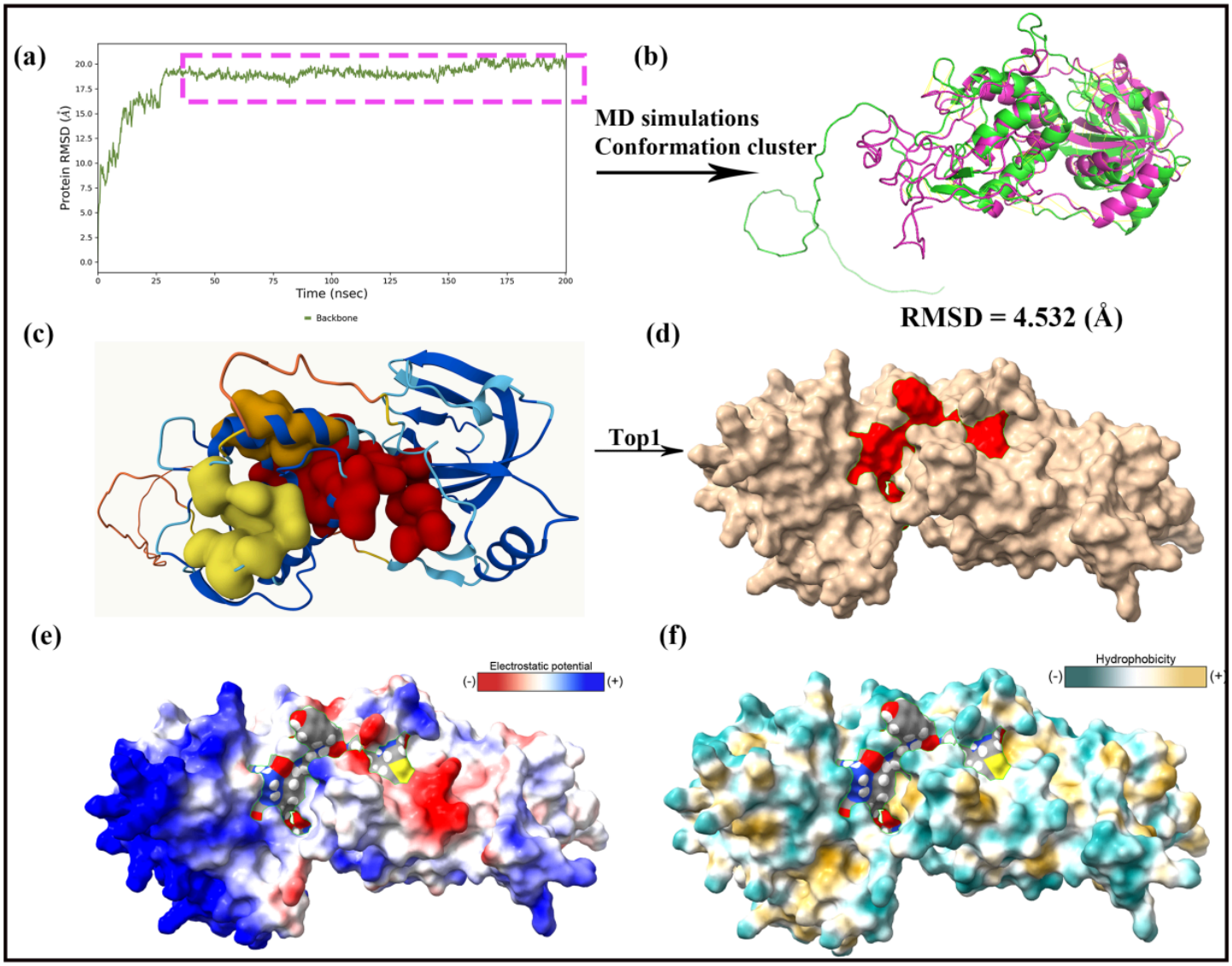


Figure 1

Predictive result of SFRP1 protein. (**a**) The RMSD plot of SFRP1 over the 200-ns MD simulation; (**b**) The alignment of two structures (Green: predictive SFRP1 conformation; Pink: The stable conformation of SFRP1 protein obtained from MD simulation); (**c**) Predicted active pocket (Red indicates the top-ranked prediction pocket; Yellow indicates the second-ranked prediction pocket; Brown indicates the third-ranked prediction pocket); (**d**) The top1 predicting pocket; (**e**) The electrostatic potential distribution of SFRP1 protein. (**f**) The hydrophobicity distribution of SFRP1 protein.

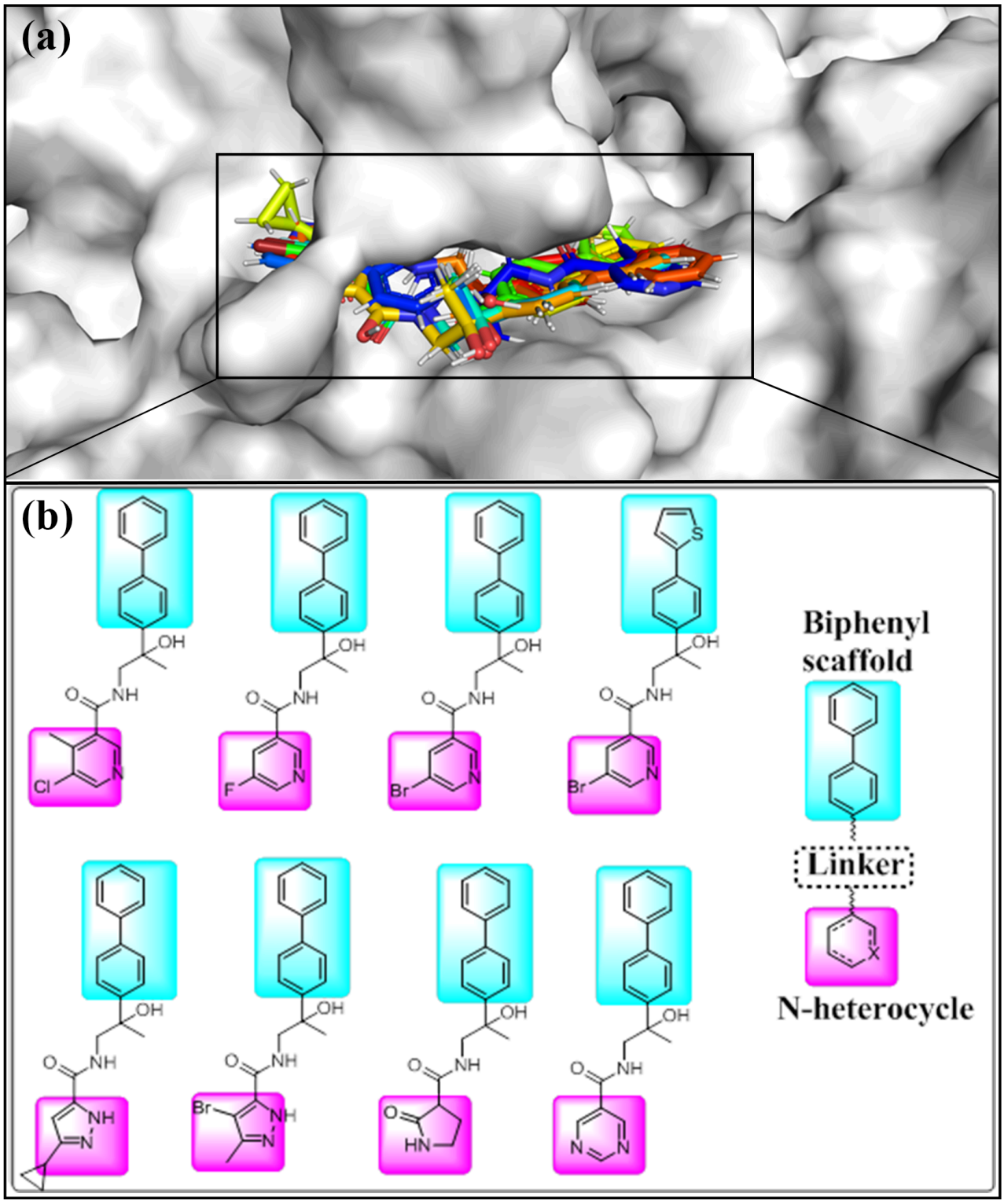
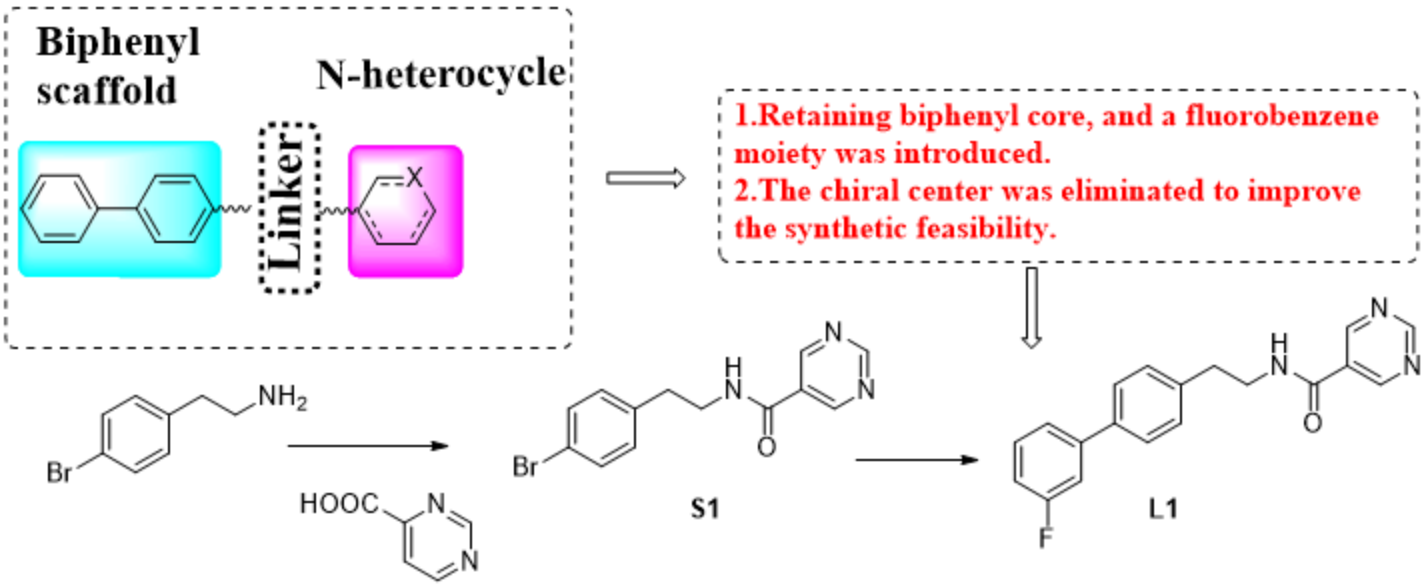


Figure 2

Results of cluster analysis



Reaction conditions: **(a)** 4-Bromophenethylamine, 5-Pyrimidinecarboxylic acid, HOBT, EDCI, CH_2Cl_2, r.t. 24 h; **(b)** S1, 3-fluorophenylboronic, K_2CO_3, $Pd(pph_3)_4$, 1,4-Dioxane, H_2O, N_2, 120 °C, 18 h.

Figure 3

The design and synthesis scheme of target product

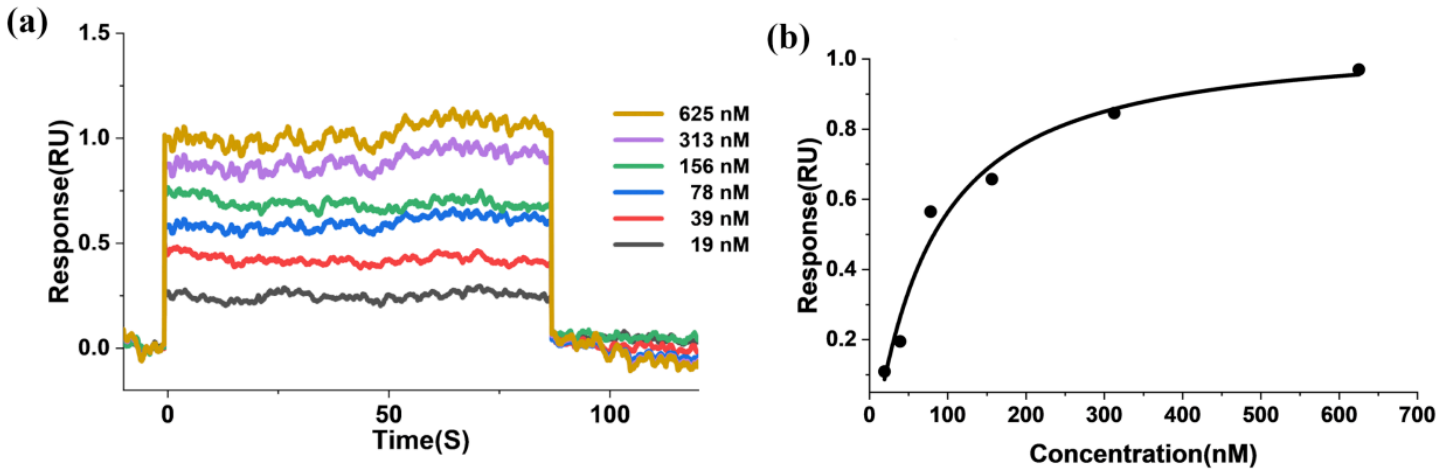


Figure 4

The result of SPR. (**a**) The real-time surface plasmon resonance (SPR). (**b**) Equilibrium affinity fitting curve.

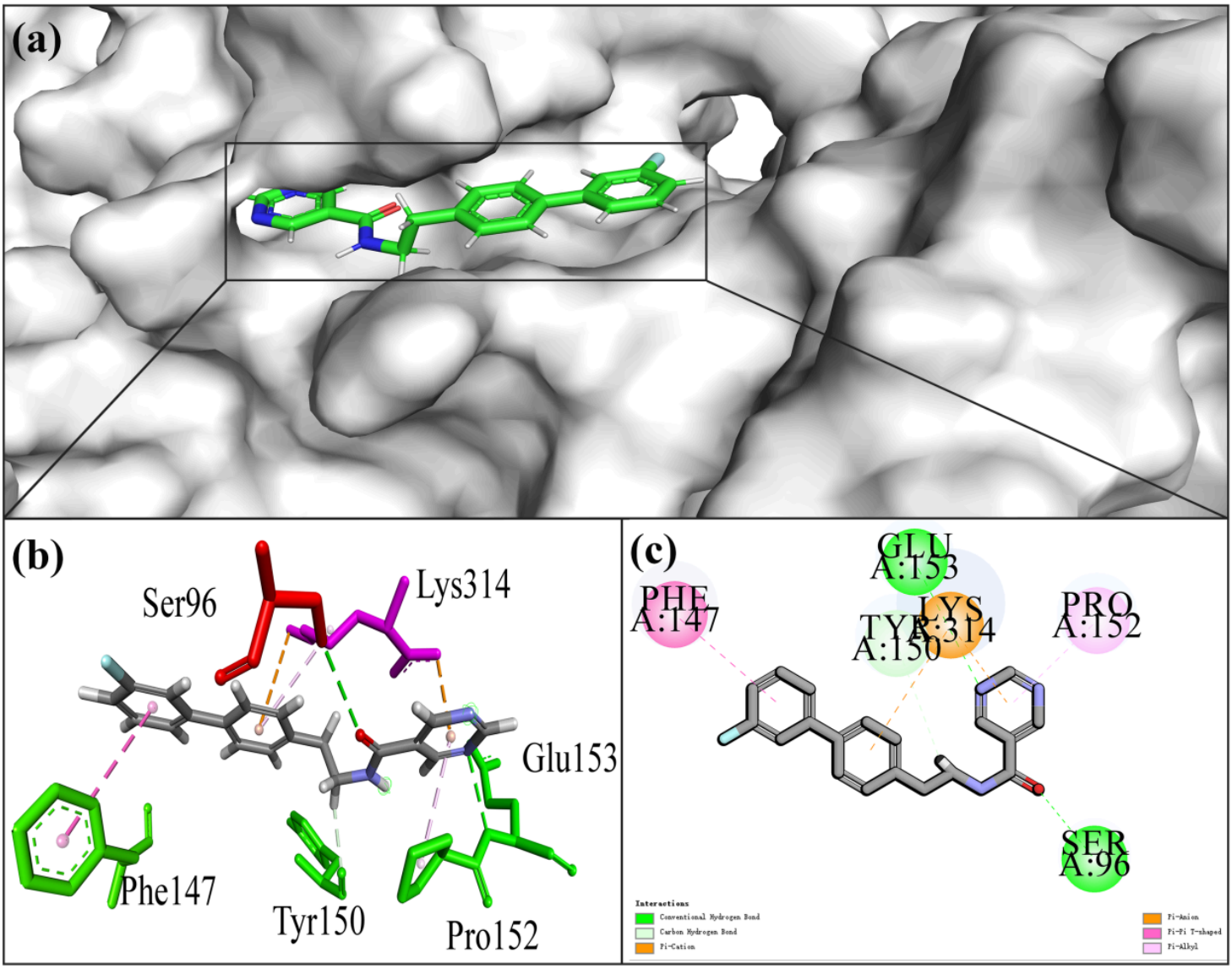


Figure 5

Docking results diagram of **L1** with SFRP1. (**a**) The pose of **L1** in active pocket; (**b**) Active sites of amino acid residues represented in parent color line model; (**c**) 2D diagram of interactions.

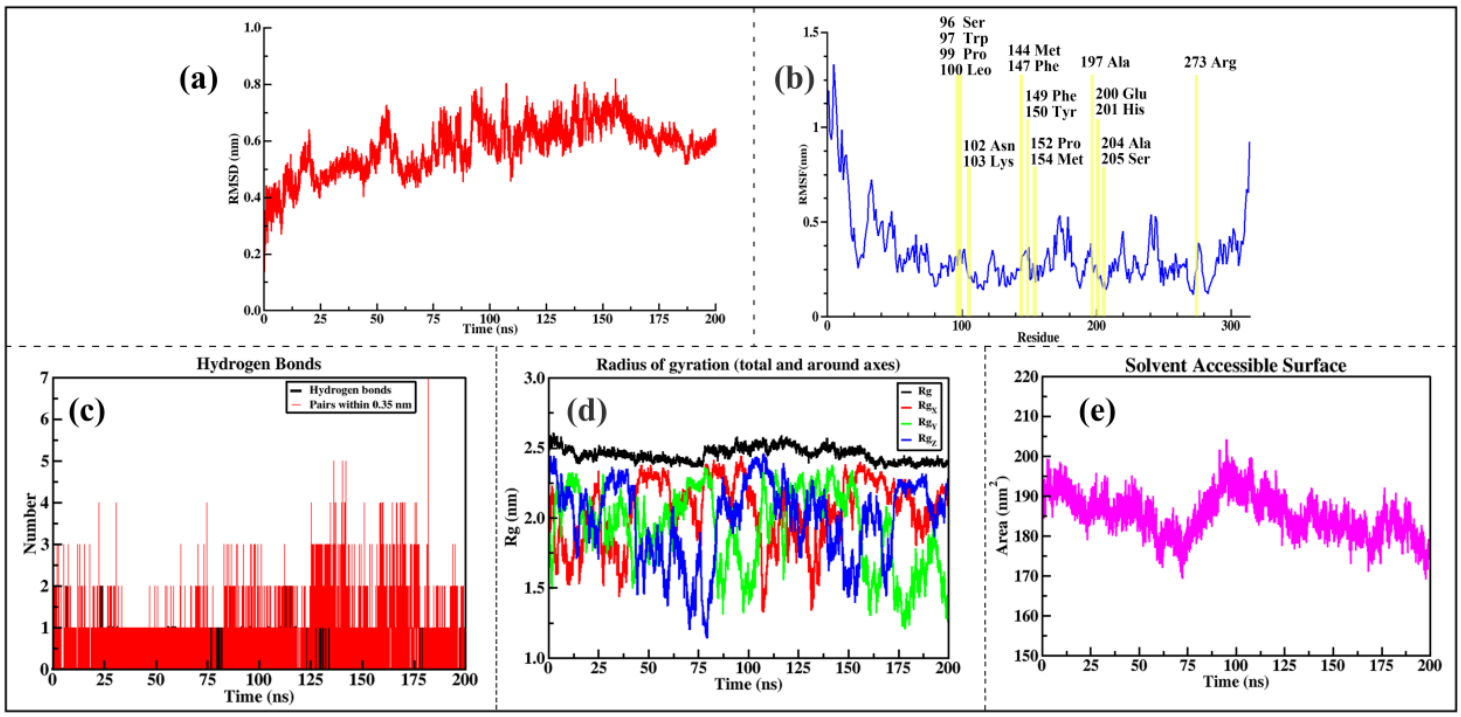


Figure 6

The result of MD simulation. (**a**) RMSD plot of SFRP1-**L1**complex; (**b**) RMSF plot of SFRP1-**L1** complex; (**c**) Hydrogen bonds of SFRP1-**L1**complex; (**d**) Rg of SFRP1-**L1**complex; (**e**) SASA plot of SFRP1-**L1** complex;

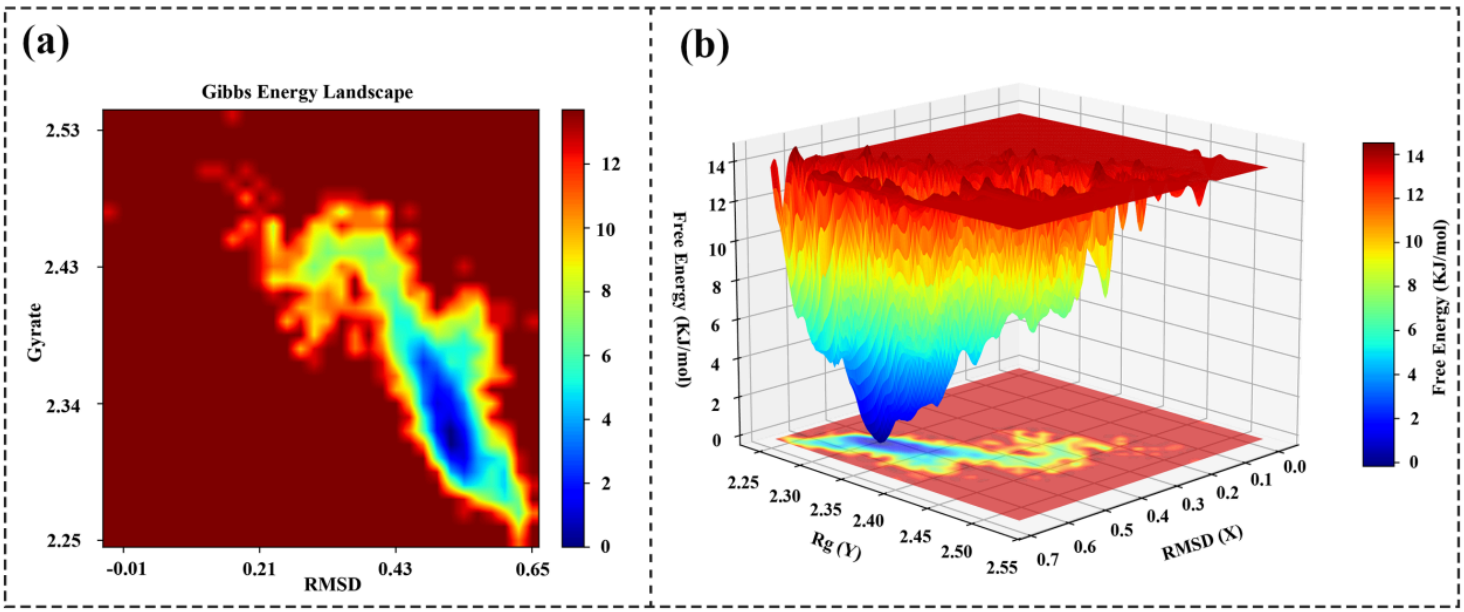


Figure 7

FEL of SFRP1-**L1** complex. (**a**) 2D Gibbs energy landscape; (**b**) 3D Gibbs energy landscape, High energy (red color), intermediate energy (yellow and green) and low/stable energy (lightto-dark blue color) levels

were shown in graph.

Supplementary Files

This is a list of supplementary files associated with this preprint. Click to download.

- Supplementaryinformations.docx